Electronic Supplementary Material (ESI) for Nanoscale.

Supporting Information

Light Intensity Field Enhancement (LIFE) Induced Localized Edge Abrasion of Silica-Coated Silver Nanoprisms

Rijil Thomas,[a] Soo Zeng Fiona Phua,[b] Sivaramapanicker Sreejith,*[,c] Yanli Zhao,*[,b] and Cheong Boon Soh*[,a]

[a]School of Electrical and Electronic Engineering, Nanyang Technological University, 50 Nanyang Avenue, Singapore, 639798, Singapore.

[b]Division of Chemistry and Biological Chemistry, School of Physical and Mathematical Sciences, Nanyang Technological University, 21 Nanyang Link, 637371, Singapore.

[c]Centre for Advanced 2D Materials and Graphene research Centre, National University of Singapore, 117543, Singapore.

S1. Radius of Curvature (ROC) Analysis

Analytical models and solutions of scattering and absorption of electromagnetic (EM) waves can be estimated only for simple and symmetric particles like spheres.[1] For nanoparticles like rods and prisms, numerical techniques should be used. In such studies with nanoparticle models using ideal sharp edges in numerical calculations were proven to produce erroneous results against nanoparticle models with corner and/or edge smoothening.[1–3] Even though only the finite radius of curvature (ROC) at the three corners was considered in few of these studies,[2,3] the melting ice model[1] which considered smoothening of both the corners as well as edges was close to the real case. So, we initially performed a simulation analysis of corner and edge smoothening individually on the nanostructure.

S1.1. Edge and Corner Smoothening – Geometry

A 10 nm thick silica coated silver nanoplate ($AgNPr@SiO_2$) of 110 nm side (10 nm thickness) and using different ROC combinations of corners and edges were considered for our study. **Figure S 1** shows different geometries of AgNPr used as core structures in our hetero-nanostructures.

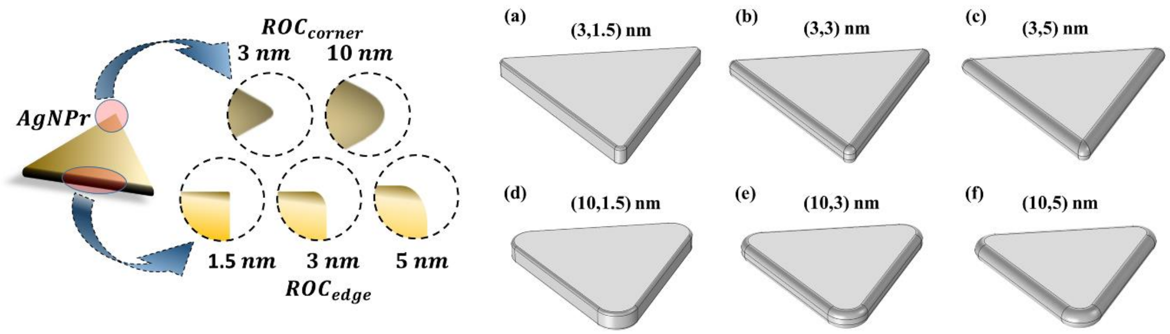

Figure S 1. Geometry of AgNPr with corner ROC and edge ROC formatted as (ROC_{corner}, ROC_{edge}) nm: (a) (3,1.5) nm, (b) (3,3) nm, (c) (3,5) nm, (d) (10,1.5) nm, (e) (10,3) nm and (f) (10,5) nm.

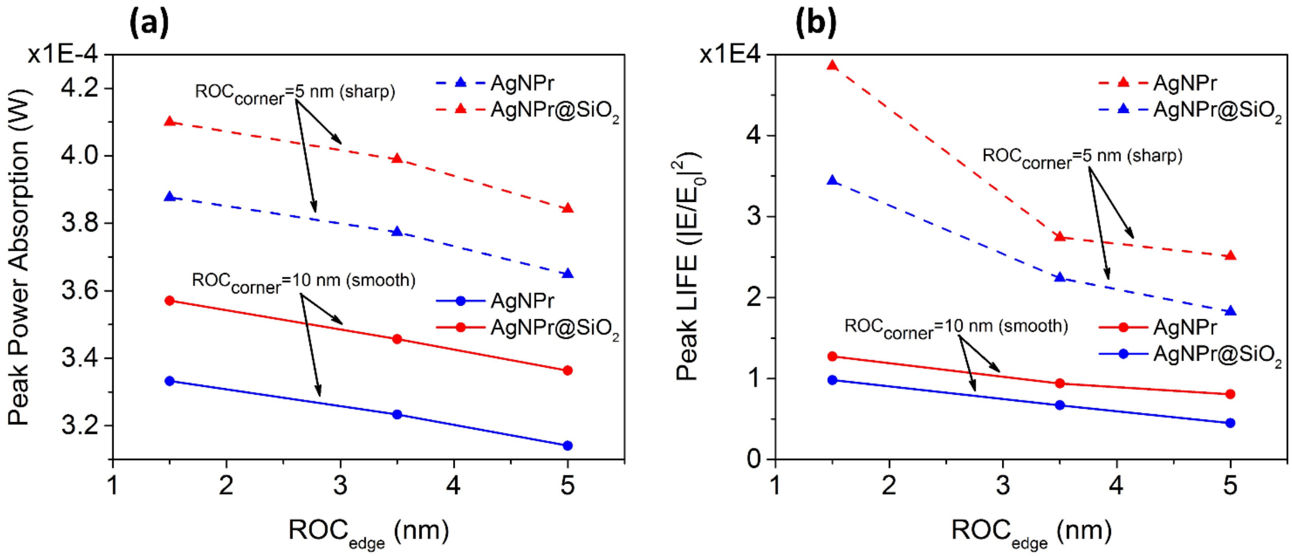

Figure S 2. Comparison of (a) absorption peak and (b) intensity enhancement peak of AgNPr and AgNPr@SiO$_2$ nanostructures with varying ROC_{corner} and ROC_{edge}.

We have considered a nanosecond pulse of duration t_p $(7\ ns)$ and fluence $7\ mJ/cm^2$ as the excitation source. The absorption profile and intensity enhancement of the nanostructure is then numerically calculated using FEM and estimated parameter is power absorbed (P_{abs}). The power absorbed by the particle comprises mainly resistive heating of the particle during the laser irradiation,[4] which is directly proportional to the absorption cross section (α_{abs}) by $P_{abs} = I_g \alpha_{abs}$,[5] where I_g is the light intensity. Similar to the observations from previous studies[1–3] our calculations show a reduction in absorption with smoothening or increasing ROC. **Figure S 3** shows the calculated absorption profile of bare AgNPr and AgNPr@SiO$_2$ respectively. In addition to the proportional reduction in absorption, a blue shift is clearly visible from the full absorption spectra profile and can be attributed to the reduction in effective side length of the nanoplate as the ROC is increased for our specific triangular geometry. We also studied the variation of light intensity field enhancement (LIFE) in these nanostructures (**Figure S 4**). It is defined as the ratio of electric field intensity $(|E|^2)$ inside the nanostructure when laser irradiated to that of ambient medium electric field intensity $(|E_0|^2)$ used to excite the nanoparticle. The maximum LIFE can be observed near the corners which is corresponding to the hotspot formed. **Figure S 2**(a) and (b) shows the variation of absorption and LIFE peaks with smoothening. Additionally, the electric field can be related to the intensity using the Poynting vector relation $I_{av} = (E \times H^*)/2$,

$$I = \frac{E^2 n c \varepsilon_0}{2} \tag{E1}$$

where, n is the refractive index of silica at irradiating wavelength, c is the speed of light, ε_0 is the permittivity of free space and I is the intensity of laser (fluence per unit pulse width), Using intensity I from the irradiating conditions mentioned above and n as the refractive index of water, we get an input ambient electric field (E_0) of 2.4 MV/m.

S1.2. Absorption Profile – Radius of Curvature (ROC) Analysis

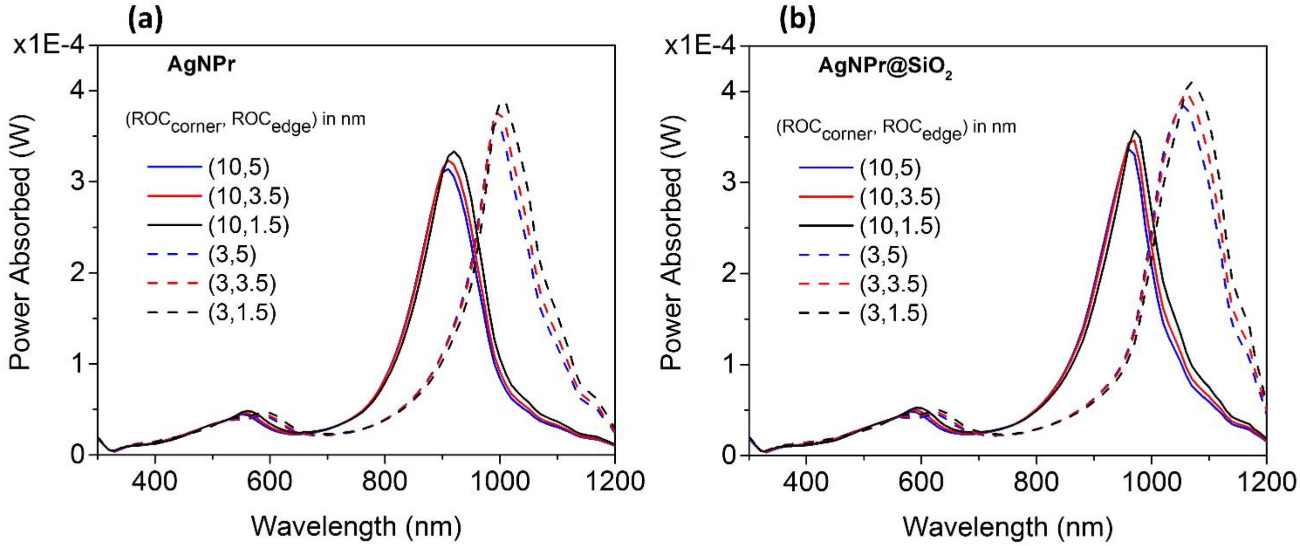

Figure S 3. Absorption profile of (a) AgNPr and (b) AgNPr@SiO2 calculated using FEM.

Absorption profile of the bare silver nanoplate (AgNPr) and silica coated silver nanoplate (AgNPr@SiO₂) were calculated for different corner ROC and edge ROC using finite element method (FEM). **Figure S 3** shows the comparison of power absorbed by these nanostructures. A blue shift with increasing ROC_{corner} and ROC_{edge} is obvious. But the effect of increasing ROC_{corner} is dominant than that of increasing ROC_{edge}.

S1.3. Maximum Light Intensity Field Enhancement (LIFE) Profile – Radius of Curvature (ROC) Analysis

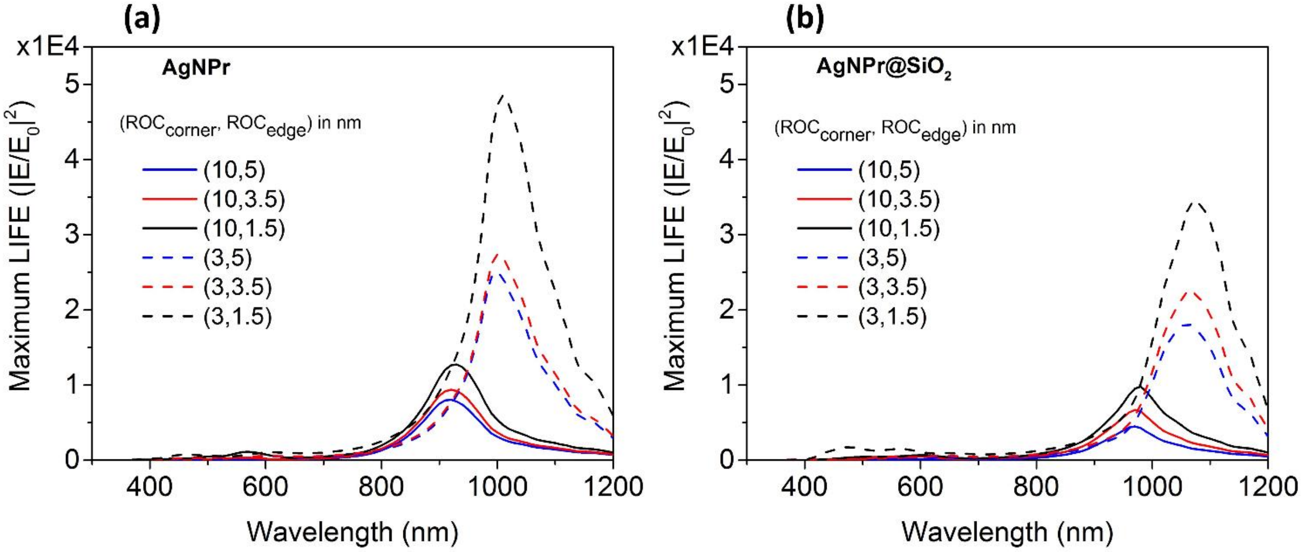

Figure S 4. Maximum LIFE of (a) AgNPr and (b) AgNPr@SiO2 calculated using FEM.

LIFE of the bare silver nanoplate (AgNPr) and silica coated silver nanoplate (AgNPr@SiO$_2$) were calculated for different corner ROC and edge ROC using finite element method (FEM). **Figure S 4** shows the comparison of maximum LIFE, which is near the corners of the nanostructures. Similar to that of absorption, a blue shift with increasing ROC_{corner} and ROC_{edge} can be seen while the effect of increasing ROC_{corner} being dominant than that of increasing ROC_{edge}.

S2. Graphene Oxide Wrapping on Silica Coated Silver Nanoprisms (AgNPr@SiO$_2$)

For a sphere, the effective bending and change in propagation direction of the EM wave caused by the ambient environment (GO coating) would not change the polarizability of the nanoparticle. The symmetry of the sphere in all directions will produce the same dipole moment for EM waves incident from any direction. The propagation and direction of incidence should not be misinterpreted as classical ray optics but rather a change in direction of electric field oscillation and an effective change in propagation direction for only a small space where nanoparticle exists. For a nanoprism, due to its non-symmetrical/non-spherical geometry, the bending of field (bending expected to be high due to the high value for real part of refractive index of GO coating) as mentioned before will cause a change in polarizability due to its change in shape and effective area the field propagates through. An illustration of above explanation can be found in **Figure S 5**. Here, line n corresponds to the direction of electric field oscillation incident on nanoparticle normally and thus without any bending. Meanwhile, the line o corresponds to the direction of electric field oscillation incident at an oblique angle which has changed its direction of oscillation. Moreover, the presence of GO (complex dielectric permittivity) may induce scattering. For a large size particle as a nanoprism, the role of extra layer of GO as a scatterer might be significant compared to that of small spherical nanoparticles.

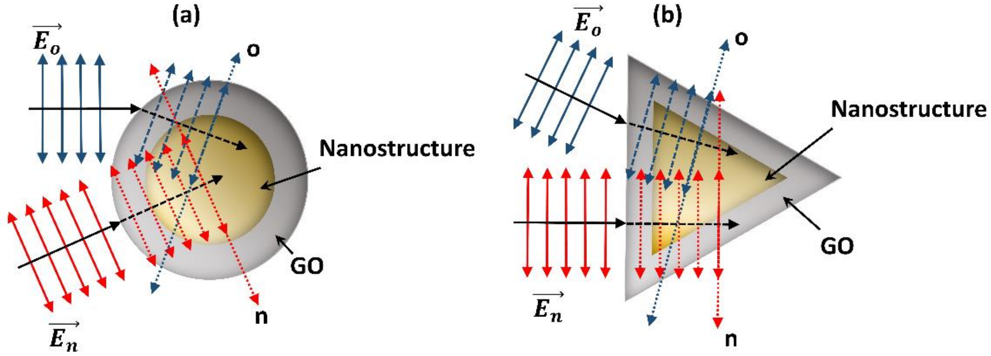

Figure S 5. Illustration of the interaction of EM field with GO wrapped (a) nanosphere and (b) nanoprism. $\overrightarrow{E_n}$ is the field incident normal to the structure and $\overrightarrow{E_o}$ is the field incident at an oblique angle. Line n and Line o shows the corresponding direction of polarization.

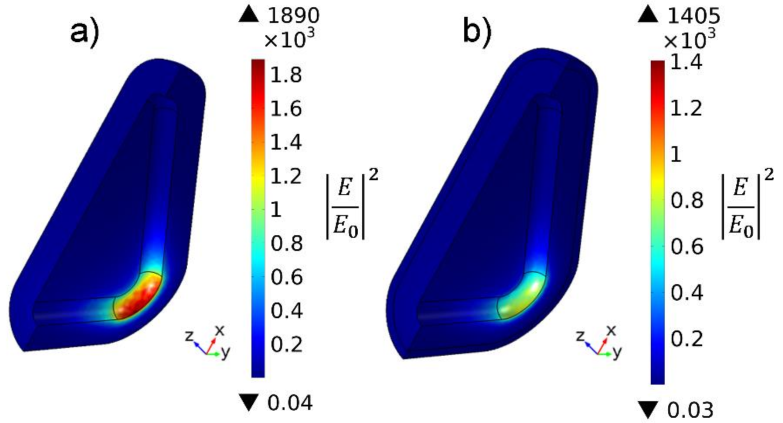

Figure S 6. FEM simulation results illustrating the reduction in LIFE near corners between silver-silica interface when wrapped with GO. (Excitation at 900 nm). The images correspond to (a)AgNPr@SiO$_2$ and (b)GO- AgNPr@SiO$_2$.

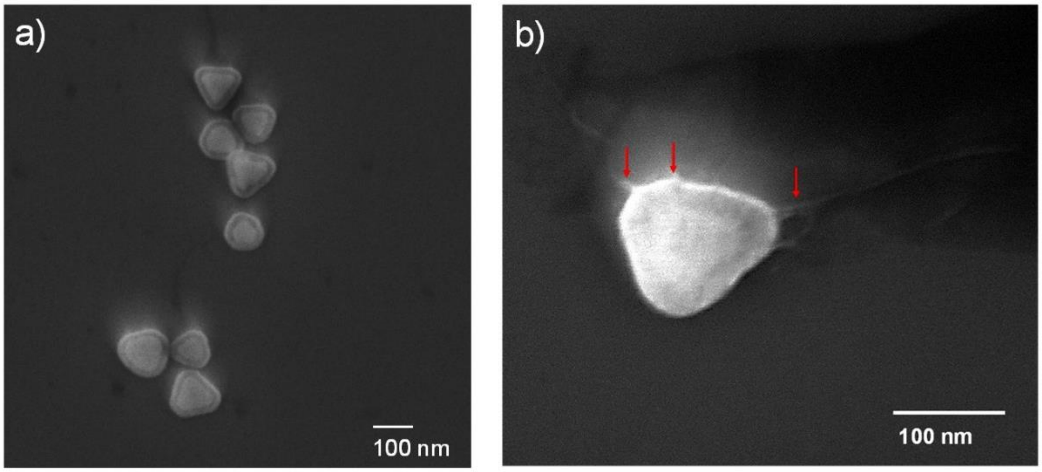

Figure S 7. Field emission scanning electron microscope (FE-SEM) images of AgNPr@SiO2 and GO wrapped AgNPr@SiO2. Red arrow indicates wrapped GO on single nanoprism surface.

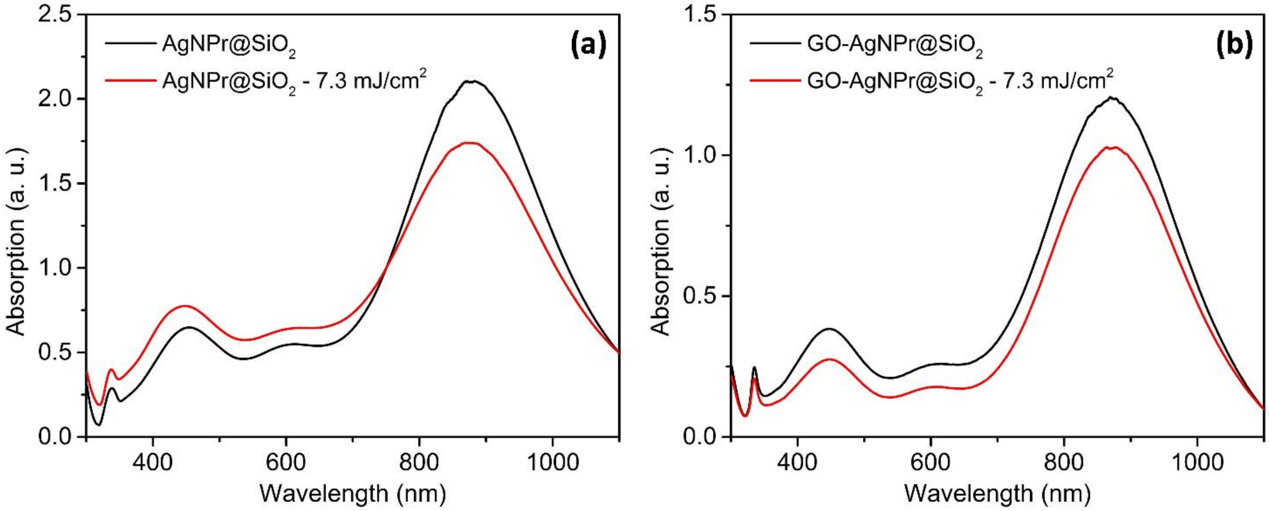

Figure S 8. Comparison of measured absorption spectra (a) AgNPr@SiO2 and (b) GO wrapped GO-AgNPr@SiO2 before and after irradiation (900 s exposure) with 7 ns pulse of fluence 7.3 mJ/cm^2 at 900 nm wavelength.

Figure S 8 clearly shows a change in absorption spectra of AgNPr@SiO$_2$ and GO wrapped AgNPr@SiO$_2$. The change in shape and broadening of spectrum of silica coated silver nanoprism (**Figure S 8** (a)) can be attributed to the change in refractive index which occurred due to the damage of environment silica matrix. Meanwhile, the preserved shape of spectrum for GO wrapped nanostructure sample (**Figure S 8** (b)) clearly indicates that no damage has occurred by laser irradiation. However, the reason for reduced value of the spectrum is unknown.

S3. Experimental Setup

S3.1 General

The nanoparticle (AgNPr@SiO_2) samples were obtained from the commercial supplier Nanocomposix and used as received. The laser excitation experiment was conducted using Opolette tunable laser (Opotek Inc. Tunable Laser Systems, Canada) as the excitation source and Thorlabs optical setup (lens, mirrors and optical table). Electronic absorption spectra were recorded on a Shimadzu UV-3101 PC NIR scanning spectrophotometer. TEM images were captured by JEOL 2010 TEM at 200kV. Zeta potential was measured by Mavern Nanosizer. Raman spectra of the nanoparticles on cleaned silicon substrate were measured with a Raman microscope (LabRAM HR, Horiba Yvon). The excitation wavelength of the irradiating light was 633 nm (He-Ne Laser, Melles Griot) and signals were collected by using a × 100 objective lens.

GO was prepared by a modified Hummer's method.[6] Graphite (0.5 g) was suspended in concentrated H_2SO_4 (15 mL) under ice bath. $KMnO_4$ (1.5 g) was gradually added to the suspension with constant stirring. The mixture was stirred at 50 °C for 3h, followed by the addition of distilled water (35 mL). After stirring for another 15 min, distilled water (150 mL) was added to terminate the reaction. 10 mL, 30% H_2O_2 was added to the suspension and the color of solution turned into bright yellow. The mixture was then washed by HCl solution (250 mL, 10%) and distilled H_2O. In order to exfoliate the oxidized graphite, the product was treated with an ultrasonic probe at 250W for 1h and centrifuged at 8000 rpm for 30 min. The supernatant was collected. The process was repeated three times and the supernatant (600 mL) was collected as GO stock suspension. GO stock suspension (100 mL) was mixed with NaOH (5 g), sodium monochloro acetate (5 g), and the mixture was sonicated for 2h to convert the OH groups into COOH groups. The mixture was then washed repeatedly with distilled water until well dispersed GO-COOH suspension was obtained. The solvent of GO-COOH suspension was changed into DMF by centrifugation and then the solution was treated with ultrasonic probe at 250 W for 1h in order to break GO sheets into a proper size for the nanoparticle wrapping application.

Figure S 9 shows the schematic setup used for our experiment. Following a laser source to excite a 7 *ns* pulsed laser of wavelength 900 *nm*, a biconvex lens was used to collimate the Gaussian laser beam. A long-pass filter of cut off 710 *nm* was used to remove any other harmonics generated by the laser source. A neutral density filter is used to control the fluence falling on the sample. A planar mirror adjusted at 45° guides the collimated Gaussian beam towards the focusing lens which is then focused into the sample.

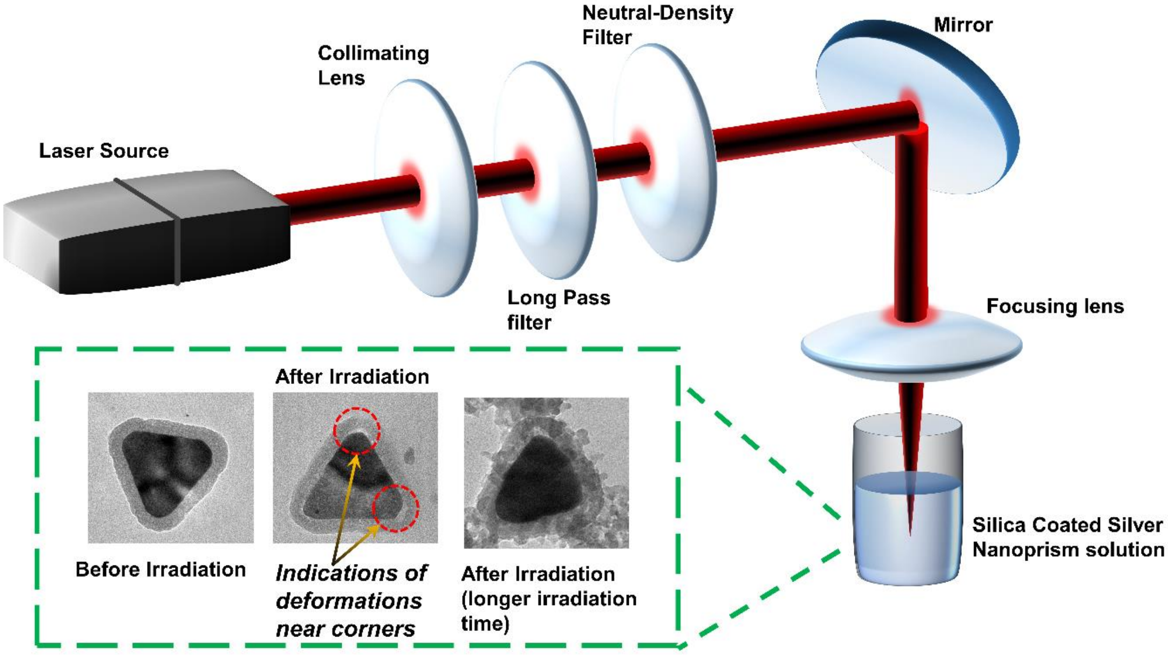

Figure S 9. Schematic of laser irradiation setup.

The following figures (**Figure S 10** and **Figure S 11**) shows the pictures of the samples used for our study for visual comparison before and after the sample being exposed to pulsed nanosecond laser.

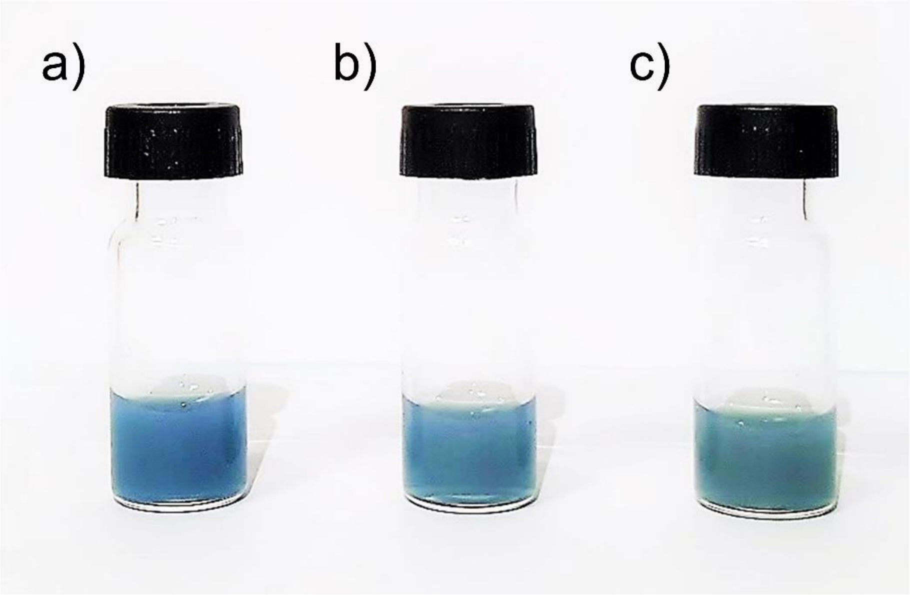

Figure S 10. (a) AgNPr@SiO$_2$ before irradiation, (b) AgNPr@SiO$_2$ after irradiation (3.6 mJ/cm^2 fluence, 7 ns pulse at 900 nm wavelength) for 900 s and (c) AgNPr@SiO$_2$ after irradiation (7.3 mJ/cm^2 fluence, 7 ns pulse at 900 nm wavelength) for 900s.

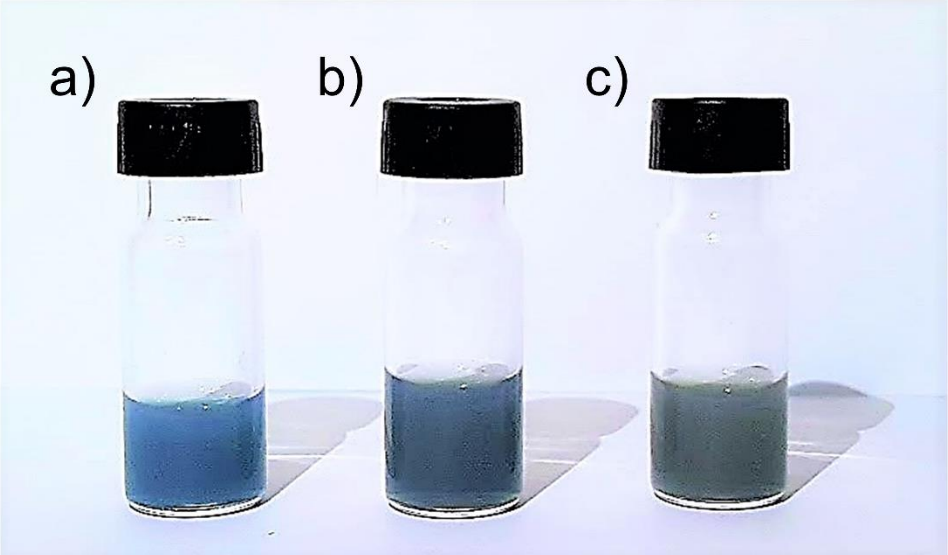

Figure S 11. (a) AgNPr@SiO$_2$ before irradiation, (b) GO-AgNPr@SiO$_2$ before irradiation and (c) GO-AgNPr@SiO$_2$ after irradiation (7.3 mJ/cm^2 fluence, 7 ns pulse at 900 nm wavelength) for 900 s.

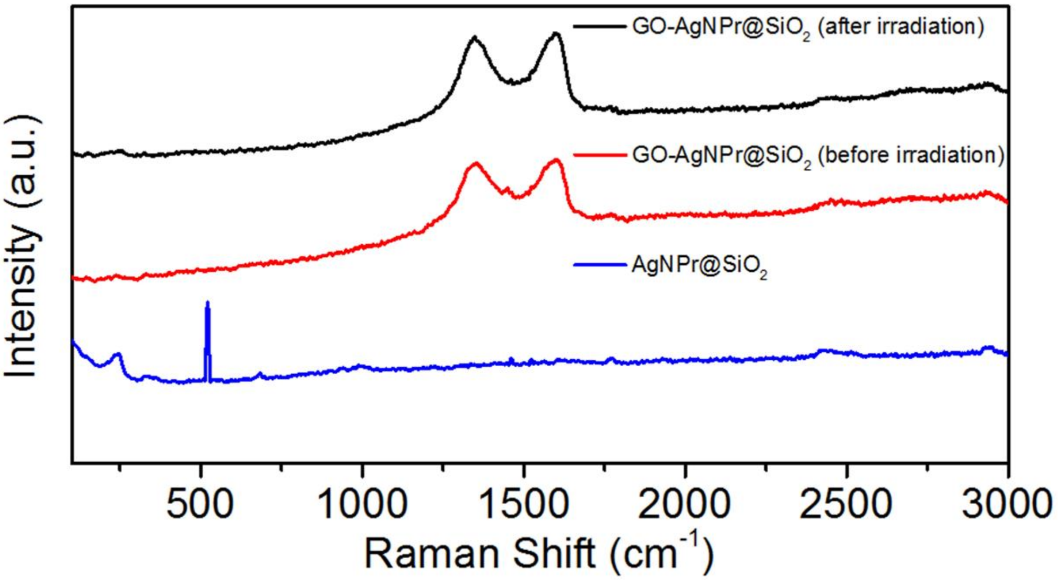

Figure S 12. Raman spectra of AgNPr@SiO$_2$ (Blue curve), GO-AgNPr@SiO$_2$ before irradiation (red curve) and after 1800 s irradiation (black curve).

S4. Fluence Calculation

S4.1 Gaussian Beam Propagation

Figure S 13 illustrates the propagation of Gaussian beam through the focusing lens which is guided into the sample. A Gaussian beam propagating through z-axis with amplitude U(r) can be expressed as:

$$U(r) = A_0 \frac{W_0}{W(z)} \exp\left[-\frac{\rho^2}{W^2(z)}\right] \exp\left[-\mathrm{jkz} - jk\frac{\rho^2}{2R(z)} + j\zeta(z)\right] \tag{E2}$$

where $W(z) = W_0\sqrt{1 + \left({}^{z}/_{z_0}\right)^2}$ is the beam radius at location z, $W_0 = \sqrt{{}^{\lambda z_0}/_{\pi}}$ is the beam waist (smallest beam radius or beam radius at location $z = 0$), $\lambda = 900\ nm$, ζ is the phase shift, A_0 is a constant, z_0 is the Rayleigh range, $R(z) = z\left[1 + \left({}^{z_0}/_{z}\right)^2\right]$ is the radius of curvature of wavefront and $\rho^2 = x^2 + y^2$. All this information can also be contained using the representation of q-parameter where:

$$q(z) = \mathrm{z} + \mathrm{jz_0} \tag{E3}$$

or equivalently

$$\frac{1}{q(z)} = \frac{1}{R(z)} - j\frac{\lambda}{\pi W^2(z)} \tag{E4}$$

Starting at the interface of focusing lens, the q-parameter of the beam inside the sample can be estimated using the transmission matrix (ABCD matrix) for Gaussian beam.

$$M = M_{sample} \times M_{free} \times M_{lens} = \begin{bmatrix} A & B \\ C & D \end{bmatrix} \tag{E5}$$

where M is the total transmission matrix, M_{lens} is the matrix for transmission through a thin lens, M_{free} is the matrix for free space propagation after the lens and before entering the sample and M_{sample} is the matrix for refraction at the planar boundary between air and sample.

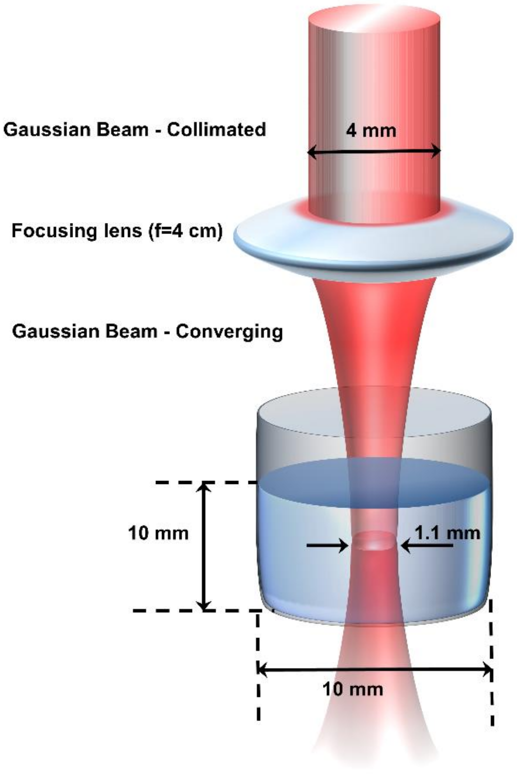

Figure S 13. An illustration to estimate fluence on the sample.

$$M_{lens} = \begin{bmatrix} 1 & 0 \\ -1/_f & 1 \end{bmatrix} \tag{E6}$$

where $f = 40\ mm$ is the focal length of the focusing lens.

$$M_{free} = \begin{bmatrix} 1 & z \\ 0 & 1 \end{bmatrix} \tag{E7}$$

$$M_{sample} = \begin{bmatrix} 1 & 0 \\ 0 & {n_{air}}/{n_{sample}} \end{bmatrix} \tag{E8}$$

where $n_{air} = 1$, and $n_{sample} = 1.33\ (= n_{water})$ are the respective refractive indices. The $1\ mg/mL$ AgNPr@SiO₂ sample is diluted with 1:19 parts water to get $0.05\ mg/mL$ and hence, the sample refractive index is approximated to that of water. Then total transmission matrix M is calculated by substituting equations E6-E8 in equation E5.

Now for input q-parameter q_I, since the beam is considered collimated, radius of curvature of wavefront $R(z) = \infty$ and waist radius $W(z)$ was found to be $\sim 2\ mm$. Using equation E4, we get

$$\frac{1}{q_I(z)} = \frac{1}{\infty} - j\frac{900\ nm}{\pi(2\ mm)^2} \tag{E9}$$

$$\Rightarrow\ q_I = j13.9626 \tag{E10}$$

Output beam has a q-parameter q_T, in the sample as

$$q_T = \frac{Aq_I + B}{Cq_I + D} \tag{E11}$$

Now $W(z)$ profile inside the sample can be found using imaginary part of q_T^{-1} (from equations E4 and EE11). Once the $W(z)$ is estimated, the cross-sectional area and thus the fluence $F(z)$ at each height inside the sample can be estimated. Then the average fluence the sample receives is the calculated as

$$F_{av} = \frac{1}{h}\int F(z)\,dz \tag{E12}$$

where $h = 10\ mm$ is the height of the sample.

S4.2 Depth Resolved Fluence

Since there is an absorbance μ_a for the solution, fluence reaching into depths reduces and the depth-resolved optical fluence can be found by modifying equation E12 to the following[7]

$$F_{av} = \frac{1}{h}\int_0^h F(z)exp(-\mu_a(\lambda)z)dz \tag{E13}$$

where $\mu_a = 93.47\ cm^{-1}$ is maximum absorbance or Optical Density (OD) given for the 1 mg/mL solution at 900 nm. Using Beer Lambert's Law

$$\mu_a \propto concentration\ of\ the\ solution \tag{E14}$$

Hence for 0.05 mg/mL solution, OD is reduced by 20 times to $\mu_a = 4.6734\ cm^{-1}$. Finally, this gives an average fluence of $F_{av} = 7.3\ mJ/cm^2$ inside the sample. This is for the case where ND filter is not used in the setup. By using an ND filter of 50% transmission as shown in **Figure S 9** we obtained a fluence of 3.6 mJ/cm^2, which is around half of the initial fluence. We conducted our experiments using these two values of fluence.

S4.3 Transmission Coefficient

Finally, the ambient electric field E_0 is the calculated using Poynting vector relation $I_{av} = (E \times H^*)/2$, i.e., $I = (E^2\ nc\varepsilon_0)/2$ and including a small correction factor of transmission coefficient τ to account of reflection and transmission of light when travelling from air to water. The corrected electric field inside the sample will be $E' = \tau E$, where

$$\tau = \frac{2n_{air}}{n_{sample} + n_{air}} \tag{E15}$$

giving a value of ~86% transmission ($\tau = \sim 0.86$).

S5. Laser Induced Damage on Silica

S5.1 Laser Induced Damage Mechanisms in Literature

The laser induced damage on silica can be either by direct irradiation or by foreign material inclusions induced via plasmonic interaction. Numerous studies have been conducted extensively on laser induced damage and dielectric breakdown on silica and other oxides since decades.[8–13] There are several proposed postulates for the damage process including avalanche ionization (impact ionization), multiphoton ionization (MPI), tunneling, etc. The foremost proposed theory is avalanche which can happen in thin oxides under the influence of electric field and short pulse regime where as in ultrashort pulse regime like femtosecond pulses, multiphoton ionization alone is capable of producing high electron density to reach plasma critical density.[9] Mechanisms for optical breakdown for sub-picosecond pulses are well known and laser induced damage thresholds (LIDT) provide deterministic values as the lattice has no time to respond during the pulse.[9,13–15] Hence, no effect of lattice scattering, thermal or mechanical stress is accountable in this case.[9] On the contrary, for longer pulses like nanosecond and continuous wave (CW), threshold estimation is not reliable and vary by a factor of more than 100.[10] Here the mid-gap states due to defects plays a role where these states get occupied when the material relaxes during long pulses.[14] Additionally, little is known about the optical properties of these defects.[16] Moreover, all the above studies observe the damage process on a microscopic scale on bulk surfaces or thin films. This may be the reason of very high but inconsistent values of reported threshold fluence of the order $10^4\ J/cm^2$. The onset of damage on nanoscale might give even less varying LIDT.

S5.2 Challenges in Determining a Threshold (LIDT)

Practically, there are many possibilities to considered which might raise a challenge in finding an exact threshold where the silica material breakdowns. The laser induced damage on silica has never reported a reliable threshold for nanosecond pulses due to mid-gap defect states. In nanoparticles, we do not have much information about the number of defect states and thus their effects during nanosecond and longer pulses. The interface between the metal and the silica shell are likely to have defects, especially near the corners due to high probability for imperfections. Moreover, the damage threshold can be shape and size dependent. In our studies, the effect of electric field is on localized spots of triangle shell shaped silica. Another factor which poses the challenge is the deviation of estimated shape by corner and edge smoothening using ROC from the synthesized nanoprisms. Finally, the difficulty in theoretical estimation also arises from coupling several significant temperature dependent phenomena which are dependent on each other as elaborated in our previous studies.[17]

S5.3 Laser Induced Damage Mechanism in Nanoparticles (Silica Coated Silver Nanoprisms)

As mentioned earlier, the metal-silica interface is highly likely to contain defect states near the corners. Initially, for a transparent solid like silica, the charge carrier density can be assumed to be around at least $10^8\ cm^{-3}$ at room temperature.[18] But this means only a negligible amount of initial seed electrons to initiate the damage process in the silica nanovolume. In spite of the large fluence threshold of order $10^4\ J/cm^2$ reported in literature and models fits based on damages observed on microscale, a low threshold of order $10\ J/cm^2$ was used to etch out silica nanoballs which is an observation of damage in nanoscale triggered with lower fluences.[19] This is an indication that MPI can be initiated in this range. In our studies, we also estimated an equivalent fluence of the same order ($7.3 - 14.6\ J/cm^2$) corresponding to the enhanced field near the corners. So, from this observation, we propose that fluence of order $10 J/cm^2$ is enough to initiate MPI to seed avalanche. Additionally, upon irradiating $7.3\ mJ/cm^2$ fluence, the temperature of the metal can rise up to $600\ K$, which was found using FEM method (COMSOL Multiphysics). This temperature exists nearby the metal nanoparticle can control conduction band (CB) electrons from relaxing down to deep traps or valence (VB), reducing the threshold for remaining pulse. Then for the remaining pulse duration as well as further pulses, impact ionization seeded by these electrons can raise the electron density in the CB to reach critical density. As well known, once the critical density is reached, the plasma frequency matches the laser frequency making the material strongly absorbing. This enables the easy deposit of energy altering the properties of material.[16] Furthermore, we continued to repeat the experiment using longer irradiation time allowing more pulse to excite the nanoparticles. Here, the TEM images of $3.6\ mJ/cm^2$ irradiated sample still showed no changes. At the same time, $7.3\ mJ/cm^2$ irradiated sample had undergone structural changes, but the impact was higher than the previous results. Silica shell was damaged and ruptured. Moreover, as the irradiation time is increased, the damage impact was observed to increase due to decreasing threshold. It is known that multiple exposures will lower the threshold damage, which might be due to incubation.[16] This phenomenon implies laser induced modifications like the introduction of more defects and occupying existing defects and traps, weakening the system to further pulses.

S5.4 Results-Damage Ratio

Figure S14 summarize our results comparing the damage ratio (damage area to silica area) on AgNPr@SiO₂ upon 300 s and 900 s irradiations. Analysis for 1800 s irradiation is insignificant since the damage area could not be properly segmented.

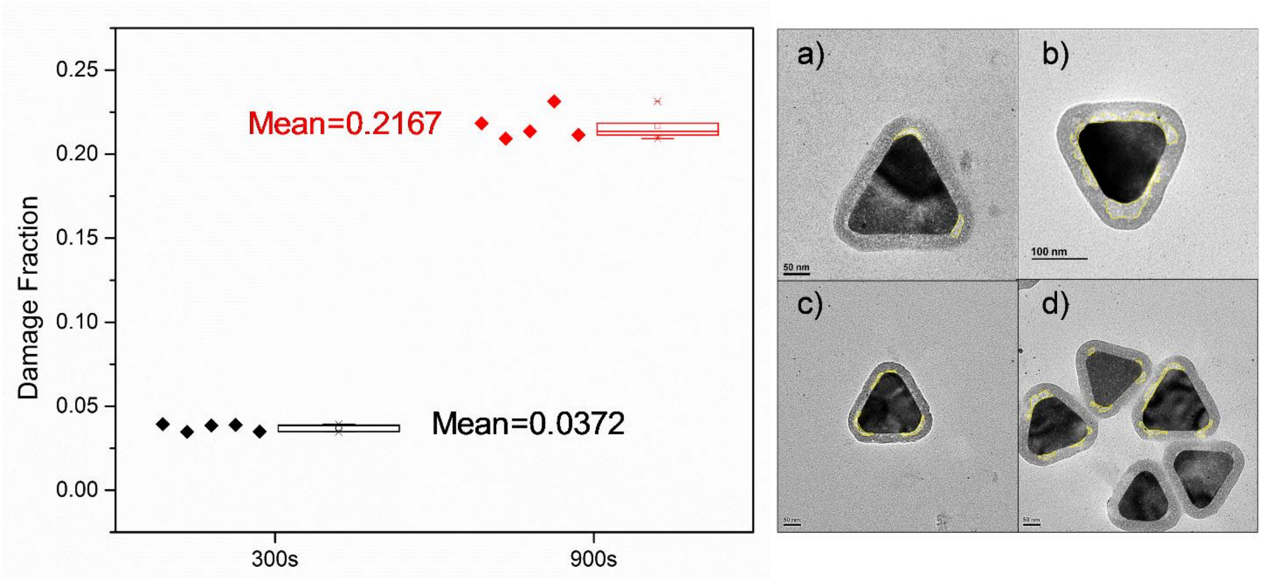

Figure S14. Box plot comparing the damage ratio of 300 s and 900 s irradiations on AgNPr@SiO2 using 5 areas of TEM images. The results marked in black corresponds to 300 s irradiations and red corresponds to 900 s irradiations. The right image shows 2 pairs of TEM image of (a, c) 300 s irradiation and (b, d) 900 s irradiation. The abrasions are highlighted in yellow. Values estimated using ImageJ software.

Reference

1 J. Jayabalan, A. Singh and R. Chari, *Appl. Phys. Lett.*, 2010, **97**, 41904.
2 B. Grześkiewicz, K. Ptaszyński and M. Kotkowiak, *Plasmonics*, 2014, **9**, 607–614.
3 T. Mori, K. Yamaguchi, Y. Tanaka, Y. Suzaki and M. Haraguchi, *Opt. Rev.*, 2016, **23**, 260–264.
4 A. Hatef, B. Darvish, A. Dagallier, Y. R. Davletshin, W. Johnston, J. C. Kumaradas, D. Rioux and M.

Meunier, *J. Phys. Chem. C*, 2015, **119**, 24075–24080.

5 O. Ekici, R. K. Harrison, N. J. Durr, D. S. Eversole, M. Lee and A. Ben-Yakar, *J. Phys. D. Appl. Phys.*, 2008, **41**, 185501.

6 W. S. Hummers and R. E. Offeman, *J. Am. Chem. Soc.*, 1958, **80**, 1339–1339.

7 J. Wang, T. Liu, S. Jiao, R. Chen, Q. Zhou, K. K. Shung, L. V. Wang and H. F. Zhang, *J. Biomed. Opt.*, 2010, **15**, 21317.

8 C. M. Osburn and E. J. Weitzman, *J. Electrochem. Soc.*, 1972, **119**, 603.

9 B. C. Stuart, M. D. Feit, S. Herman, A. M. Rubenchik, B. W. Shore and M. D. Perry, *Phys. Rev. B*, 1996, **53**, 1749–1761.

10 A. V Smith and B. T. Do, *Appl. Opt.*, 2008, **47**, 4812.

11 G. Mann, S. Pentzien and J. Krüger, *Appl. Surf. Sci.*, 2013, **276**, 312–316.

12 J. Han, *Opt. Eng.*, 2012, **51**, 121809.

13 S. G. Demos, R. A. Negres, R. N. Raman, A. M. Rubenchik and M. D. Feit, *Laser Photon. Rev.*, 2013, **7**, 444–452.

14 W. Rudolph, L. Emmert, Z. Sun, D. Patel and C. Menoni, in *SPIE Proceedings*, eds. G. J. Exarhos, V. E. Gruzdev, J. A. Menapace, D. Ristau and M. Soileau, 2013, vol. 8885, p. 888516.

15 R. R. Gattass and E. Mazur, *Nat. Photonics*, 2008, **2**, 219–225.

16 L. Emmert and W. Rudolph, in *Laser-Induced Damage in Optical Materials*, CRC Press, 2014, pp. 127–152.

17 R. Thomas, S. Sreejith, H. Joshi, S. Pedireddy, M. C. Stuparu, Y. Zhao and S. C. Boon, *J. Phys. Chem. C*, 2016, **120**, 11230–11236.

18 N. Bloembergen, *IEEE J. Quantum Electron.*, 1974, **10**, 375–386.

19 Z. Xia, D. Li, Y. Zhao and Y. Wu, *Opt. Laser Technol.*, 2013, **46**, 77–80.